Geochemical Perspectives Letters

Cerium isotopic constraints on oceanic redox conditions: Insights from first-principles calculations

H.-C. Duan, Z.-C. Xiao, F. Huang

Supplementary Information

The Supplementary Information includes:

- Theoretical Equilibrium Isotope Fractionation
- Static First-principles Calculations
- Optimised Mineral Structures
- Mass-dependent Isotope Fractionation Factors
- Mass-independent Isotope Fractionation Factors
- Tables S-1 to S-3
- Figures S-1 to S-6
- Supplementary Information References

Theoretical Equilibrium Isotope Fractionation

Mass-dependent equilibrium isotope fractionation factors ($10^3 ln\alpha_{Mass}$) between two substitution phases can be estimated by their difference in reduced partition function ratios ($ln\beta_A - ln\beta_B$) (Hoefs, 2009). The translational, rotational, and vibrational partition functions for substance A can be used to calculate β_A using the following equation:

$$\beta_A = \left[\prod_q \prod_i^{3N} \frac{u_{ih}}{u_{il}} \frac{e^{-u_{ih}/2}}{1-e^{-u_{ih}}} \frac{1-e^{-u_{il}}}{e^{-u_{ih}/2}}\right]^{1/q} \quad \text{(Eq. S-1)}$$

where h and l refer to the heavy and light isotopes, q is the number of wave vectors, $3N$ is the number of degrees of freedom for phase A, and i represents the mode number of vibrational frequencies (Bigeleisen and Mayer, 1947; Urey 1947). The u_i for the β_A calculation can be represented by the equation $u_i = hv_i/k_BT$, where h is the Planck constant, k_B is the Boltzmann constant, and v_i is the harmonic vibrational frequency of the i-th degree of freedom.

Mass-independent equilibrium isotope fractionation factors ($10^3 ln\alpha_{NVE}$) induced by the NVE can be calculated by the difference of substances A and B in the isotopic ground electronic state potential energies (Bigeleisen, 1996):

$$ln\alpha_{NVE} = 10^3 \frac{\left(E^h(A)-E^l(A)\right)-\left(E^h(B)-E^l(B)\right)}{k_B T} = 10^3 \frac{\Delta E(A)-\Delta E(B)}{k_B T} \quad \text{(Eq. S-2)}$$

where E^h(A) and E^l(A) refer to the ground electronic state potential energy of heavy and light isotopes in substance A, respectively. $\Delta E(A)$ is positively correlated with the effective density (ρ^A) in substance A and the difference in the mean-squared nuclear radii between heavy and light isotopes ($[r]^2$), which can be expressed by the following equation (Schauble, 2007; Almoukhalalati *et al.*, 2016; Dauphas and Schauble, 2016):

$$\Delta E(A) = \frac{Ze^2}{6\varepsilon_0}\rho^A[r]^2 \quad \text{(Eq. S-3)}$$

where ε_0 is the electric constant, Z is the atomic number, and e is the elementary charge. The effective density, approximated as contact density, is the electron density inside the nuclear volume, which can be approximated by the Gaussian charge distribution model (Schauble, 2007). Schauble (2013) found a good correlation of contact densities between density functional theory (DFT), Dirac-Hartree-Fock theory, and coupled-cluster methods with a regression line with a slope close to 1.00, indicating that the DFT-based contact densities we used could also provide a precise estimation of $ln\alpha_{NVE}$.

Static First-principles Calculations

The crystal structures of calcite, cerianite, percleveite, monazite, and florencite were obtained from experimental studies (Fig. S-1). The Ce^{3+}- and Ce^{4+}-doped calcite and cerianite, percleveite, monazite, and florencite structures were optimized using the Quantum Espresso package (Giannozzi *et al.*, 2017). The optimization implements the generalized gradient approximation (GGA) with an exchange-correlation function, as suggested by Perdew, Burke, and Ernzerhof (PBE; Perdew *et al.*, 1996). The PBE functional is trustworthy for geometries and vibrational frequencies of periodic boundary conditions and has been widely used in calculating isotope fractionation factors (*e.g.*, Blanchard *et al.*, 2010; Schauble 2011; Dauphas *et al.*, 2014; Young *et al.*, 2015; Pinilla *et al.*, 2021; Rabin *et al.*, 2021, 2023; Duan *et al.*, 2023). K-points in the Brillouin zone with N1×N2×N3 dense meshes were estimated based on crystal sizes (Table S-1). Although the band gap energy of the GGA+U method is closer to that of the experimental data, the doped U correction may alter the ground-state crystal structure (Morales-García *et al.*, 2020). The GGA+U method and higher-level hybrid functional were used to constrain the GGA results, indicating that the effect of U correction on

$ln\beta$ should be negligible (Liu *et al*., 2023; Duan and Huang, 2024). Therefore, GGA+U was not used in this study. Open-shell SCF calculations were performed because spin states may have a significant impact on the properties of transition metals, such as Fe (*e.g*., Wang *et al*., 2021).

The mass-dependent equilibrium isotope fractionation factors were calculated using ONCVPSP, a fully relativistic norm-conserving pseudopotential (Hamann, 2013). The valence electronic configurations of H, C, O, Al, Si, P, Ca, and Ce are $1s^1$, $2s^22p^2$, $2s^22p^4$, $3s^23p^1$, $3s^23p^2$, $3s^23p^3$, $3s^23p^64s^2$, and $5s^25p^65d^16s^2$ with cutoff radii of 1.03, 1.31, 1.67, 1.79, 1.95, 1.30, 1.91, and 2.55 Bohr, respectively. Convergence occurs when the total force and energy are less than 10^{-5} Ry/Bohr and 10^{-8} Ry, respectively. We set a tight cutoff energy of 90 Ry for the wavefunctions and a threshold of 10^{-12} Ry for the self-consistent field (SCF) throughout the calculations. These threshold parameters were tested for mineral calculations using Quantum Espresso (Duan and Huang, 2024). Subsequently, density perturbation functional theory (DPFT) (Baroni *et al*., 1987) was used to analyze the dynamic matrices and phonon vibration frequencies at an ultrafine SCF threshold of 10^{-14} Ry. We did not apply the scaling factor for vibrational frequencies.

The mass-independent equilibrium isotope fractionation factors induced by NVE were calculated using Pslibrary 1.0.0, fully relativistic projector augmented wave (PAW) pseudopotentials (Dal Corso, 2014), a method that can describe the interaction between electrons and nuclei (Kresse and Joubert, 1999). The valence electronic configurations of H, C, O, Al, Si, P, Ca, and Ce are $1s^1$, $2s^22p^2$, $2s^22p^4$, $3s^23p^1$, $3s^23p^2$, $3s^23p^3$, $3s^23p^64s^2$, and $5s^25p^65d^16s^2$ with cutoff radii of 0.8, 1.0, 1.0, 1.5, 1.6, 1.5, 1.2, and 1.3 Bohr, respectively. The GGA+PAW method is calibrated against all-electron relativistic Dirac-Hartree-Fock and coupled-cluster with single and double techniques, and the results are consistent with experimental data (Schauble, 2013). When spin-orbit coupling is considered, more precise results are obtained for $10^3 ln\alpha_{NVE}$ (Nemoto *et al*., 2015). Therefore, we also used spin-orbit coupling during the calculations. All threshold parameters used during $10^3 ln\alpha_{NVE}$ calculations are identical to those for $10^3 ln\alpha_{Mass}$.

Optimised Mineral Structures

Figure 1 shows the optimal structures of Ce-bearing minerals. The calculated crystal parameters of these minerals agree with the experimental data within a 1.1 % relative error, except for cerianite with a relative error of 5.2 % (Table S-1). The relative values between the optimized cell parameters are consistent with those produced by experiments. The calculated vibrational frequencies of Ce-bearing minerals are also identical to the experimental results (Fig. S-2). The linear regression between the calculated and experimental frequencies

of Ce-bearing minerals has a slope of 1.002 ± 0.003 (2σ, R^2=0.9999), indicating a 0.2% error in the calculated frequencies. At low temperatures, a n % shift in harmonic frequencies causes a n% uncertainty in $ln\alpha$ (Méheut *et al*., 2009). Therefore, the $10^3 ln\alpha_{Mass}$ of Ce-bearing minerals have a relative uncertainty of 0.3 % for the temperature intervals of interest.

To obtain an accurate estimate of equilibrium Ce isotope fractionation factors, we should consider the Ce and Na configurations in Ce-bearing calcites. For diatomic substitutions, the most reliable configurations may have the shortest distance between doped cations, such as Cu-In in sphalerite and Mg-Mg in calcite (Son *et al*., 2020; Duan and Huang, 2024). Based on this substitution rule, we constructed Ce^{3+}+Na^{+}-2Ca^{+} and Ce^{4+}-2Ca^{+} to represent the optimum configurations of Ce-bearing calcites. As Ce is a trace element in calcite, we should consider the influence of Ce concentration on equilibrium isotope fractionation factors by creating a sequence of supercells with Ce/Ca ratios varying from 1/4 to 1/64 (Table S-1). We found that Ce^{3+}- and Ce^{4+}-doped calcites have the shortest Ce-O bond length when the Ce/Ca ratio is equal to 1/16, which might be attributed to the asymmetric extension of the supercell that results in interactions between doped Ce cations on the shortest axis.

Reduced Partition Function Ratios

To assess the influence of Ce concentration on mass-dependent $10^3 ln\beta_{Mass}$, we compare $10^3 ln\beta_{Mass}$ with different Ce/Ca ratios at 300 K. In Ce^{3+}-doped calcites, $10^3 ln^{142/136}\beta_{Mass}$ increases from 2.58 to 2.89‰ when Ca/Ce increases from 4 to 48 and then converges at 2.90‰ as Ca/Ce increases from 48 to 64 (Fig. 1). In Ce^{4+}-doped calcites, $10^3 ln^{142/136}\beta_{Mass}$ increases from 2.13 to 3.17‰ as Ca/Ce increases from 4 to 48 and converges at 3.23‰ when Ca/Ce is 64. Furthermore, $10^3 ln^{138/136}\beta_{Mass}$ and $10^3 ln^{142/140}\beta_{Mass}$ has the same convergence threshold as $10^3 ln^{142/136}\beta_{Mass}$ in the Ce^{3+}- and Ce^{4+}-doped calcites. The value of $10^3 ln\beta_{Mass}$ is negatively correlated with the bond length of Ce-O in Ce-bearing calcites (Fig. S-3), which is consistent with the observation of In-S bonds in sphalerite and of Ca-O bonds in silicates (Xiao *et al*., 2022; Duan and Huang, 2024). The polynomial regression for the temperature ($1/T^2$) dependency of $10^3 ln^{138/136}\beta_{Mass}$, $10^3 ln^{142/140}\beta_{Mass}$, and $10^3 ln^{142/136}\beta_{Mass}$ is displayed in Fig. 1. Therefore, the results obtained from Ce/Ca of 1/64 can represent optimum structures for equilibrium Ce isotope fractionation factors of Ce-doped calcites. Calcites whose Ce concentration (Ce/Ca from 1/4 to 1/48) does not converge will no longer be discussed in the following sections. For Ce-bearing minerals, both $10^3 ln^{138/136}\beta_{Mass}$, $10^3 ln^{142/140}\beta_{Mass}$, and $10^3 ln^{142/136}\beta_{Mass}$ increase in the following sequence: cerianite, florencite, monazite, percleveite, Ce^{3+}-doped calcite, and Ce^{4+}-doped calcite (Fig. S-4).

Mass-dependent Isotope Fractionation Factors

The mass-dependent equilibrium Ce isotope fractionation factors between minerals and florencite ($10^3 ln\alpha_{Mass\ Minerals/Florencite}$) were derived from the vibrational frequencies. The polynomial regression parameters for the temperature dependency of $10^3 ln\alpha_{Mass}$ are shown in Table S-2. At the same temperatures, both $10^3 ln^{138/136}\alpha_{Mass}$, $10^3 ln^{142/140}\alpha_{Mass}$, and $10^3 ln^{142/136}\alpha_{Mass}$ increase in the following sequence of cerianite, monazite, percleveite, Ce^{3+}-doped calcite and Ce^{4+}-doped calcite (Fig. S-5a, b, c). At 300 K, the Ce^{4+}-doped calcite has a value of $10^3 ln^{138/136}\alpha_{Mass}$ of 0.50‰, which is higher than that of 0.39‰ in Ce^{3+}-doped calcite. However, Ce^{4+}-doped calcite has a longer average bond length of Ce-O than Ce^{3+}-doped calcite because the lattice defect adjacent to Ce^{4+}-polyhedron may collapse, lengthening the bond of Ce^{4+}-O. A similar result is observed for $10^3 ln^{142/140}\alpha_{Mass}$ and $10^3 ln^{142/136}\alpha_{Mass}$ in the Ce^{3+}-doped calcite and Ce^{4+}-doped calcite. These results imply that the valence state may also be a controlling factor influencing mass-dependent Ce isotope fractionation factors, in addition to the bond length. When the average bond length of Ce-O increases from 2.466 to 2.568 Å in trivalent Ce minerals, such as Ce^{3+}-doped calcite, monazite, and percleveite, $10^3 ln^{138/136}\alpha_{Mass}$ and $10^3 ln^{142/136}\alpha_{Mass}$ decrease from 0.39 to 0.19‰ and 1.13 to 0.57‰, respectively. Additionally, Ce^{4+}-doped calcite has a shorter average bond length of Ce-O than cerianite, with greater $10^3 ln^{138/136}\alpha_{Mass}$ and $10^3 ln^{142/136}\alpha_{Mass}$.

Mass-independent Isotope Fractionation Factors

The mass-independent (NVE) equilibrium Ce isotope fractionation factors between minerals and florencite ($10^3 ln\alpha_{NVE\ Minerals/Florencite}$) were derived from the electron density at nuclei. The electron density is restricted to nuclei, and the electron density of Ce is several orders of magnitude greater than that of O (see Fig. S-6). Although Equation (2) predicts a positive correlation between $10^3 ln\alpha_{NVE}$ and 1/T, we still calculate a polynomial regression of $10^3 ln\alpha_{NVE}$ with a $1/T^2$ dependency for comparison with $10^3 ln\alpha_{Mass}$ (Fig. S-5d, e, f). At the same temperature, the $10^3 ln^{138/136}\alpha_{NVE}$ increases in the following sequence of monazite, percleveite, cerianite, Ce^{4+}-doped calcite, and Ce^{3+}-doped calcite. In contrast, the $10^3 ln^{142/140}\alpha_{NVE}$ and $10^3 ln^{142/136}\alpha_{NVE}$ decreases in the following sequence of monazite, percleveite, cerianite, Ce^{4+}-doped calcite, and Ce^{3+}-doped calcite. Because the $10^3 ln^{138/136}\alpha_{NVE}$ varies in a relatively narrow range, the NVE has a limited impact on the isotope fractionation between ^{138}Ce and ^{136}Ce nuclides. However, $10^3 ln^{142/140}\alpha_{NVE}$ and $10^3 ln^{142/136}\alpha_{NVE}$ varies widely and cannot be neglected relative to $10^3 ln^{142/140}\alpha_{Mass}$ and $10^3 ln^{142/136}\alpha_{Mass}$ in Ce-bearing minerals. Significant mass-independent equilibrium isotope fractionation factors between Ce-bearing minerals support this theoretical prediction (*e.g.*, Schauble, 2023).

Supplementary Tables

Table S-1 K-point grid meshes for calculations and lattice parameters of optimised crystals at 0 GPa compared with experimental data.

Minerals	Chemical formula	Space group	K-points	*a* (Å)	*b* (Å)	*c* (Å)	Mean Ce–atom bond length (Å)	Data sources
Cerianite	Ce_4O_8	Fm-3m	6*6*6	5.691	5.691	5.691	2.507	This study
				5.411	5.411	5.411	2.343	Exp.1
				0.0517	0.0517	0.0517	0.0702	Relative Error
Monazite	$Ce_4P_4O_{16}$	P121-n1	5*5*5	6.534	7.147	8.326	2.568	This study
				6.405	7.154	8.831	2.555	Exp.2
				0.0200	0.0010	0.0571	0.0054	Relative Error
Florencite	$CeAl_3(PO_4)_2(OH)_6$	R-3m	5*5*6	7.020	7.020	7.020	2.525	This study
				6.925	6.925	6.925	2.497	Exp.3
				0.0137	0.0137	0.0137	0.0111	Relative Error
Percleveite	$Ce_{16}Si_{16}O_{56}$	P-41	5*5*2	6.900	6.900	25.077	2.534	This study
				6.796	6.796	24.728	2.530	Exp.4
				0.0153	0.0153	0.0141	0.0016	Relative Error
Ce^{3+}-doped Calcite	$CeNaCa_2C_4O_{12}$	R-3c	3*8*8	13.531	6.489	6.685	2.505	This study
	$CeNaCa_6C_8O_{24}$		3*4*8	13.061	12.886	6.518	2.485	
	$CeNaCa_{14}C_{16}O_{48}$		3*4*4	12.936	12.936	12.936	2.456	
	$CeNaCa_{22}C_{24}O_{72}$		3*3*4	12.901	19.378	12.916	2.473	

	$CeNaCa_{30}C_{32}O_{96}$		2*4*5	25.820	12.907	12.896	2.471	
	$CeNaCa_{46}C_{48}O_{144}$		2*3*4	25.774	19.320	12.876	2.467	
	$CeNaCa_{62}C_{64}O_{192}$		2*2*5	25.790	25.778	12.886	2.466	
Ce^{4+}-doped Calcite	$CeCa_2C_4O_{12}$		3*8*8	13.738	6.573	6.841	2.506	
	$CeCa_6C_8O_{24}$		3*4*8	13.290	13.329	6.668	2.508	
	$CeCa_{14}C_{16}O_{48}$		3*4*4	13.053	13.053	13.053	2.460	
	$CeCa_{22}C_{24}O_{72}$	R-3c	3*3*4	12.969	19.495	12.976	2.484	This study
	$CeCa_{30}C_{32}O_{96}$		2*4*5	25.931	12.953	12.944	2.481	
	$CeCa_{46}C_{48}O_{144}$		2*3*4	25.863	19.386	12.915	2.480	
	$CeCa_{62}C_{64}O_{192}$		2*2*5	25.834	25.828	12.905	2.473	

Exp.1 Graham, 1955; Exp.2 Ni *et al*., 1995; Exp.3 Kato, 1990; Exp.4 Deng and Ibers, 2005.

Table S-2 The mass-dependent ($10^3\ln\alpha_{Mass}$) and mass-independent ($10^3\ln\alpha_{NVE}$) equilibrium Ce isotope fractionation factors of $^{138}Ce/^{136}Ce$, $^{142}Ce/^{136}Ce$, and $^{142}Ce/^{140}Ce$ with temperatures for Ce-bearing minerals relative to florencite at 0 Gpa.

Minerals	$10^3\ln^{138/136}\alpha_{Mass}$ at 300K	a	b	c	$10^3\ln^{138/136}\alpha_{NVE}$ at 300K	a	b
Cerianite	-0.03	-0.005700	0.000300	-0.000007	0.00	0.0011	$-1*10^{-16}$
Monazite	0.19	0.016800	0.000100	-0.000003	0.00	0.0003	$-3*10^{-16}$
Percleveite	0.27	0.023600	0.000080	-0.000004	0.00	0.0004	0.0000
Calcite ($Ce^{3+}NaCa_{62}C_{64}O_{192}$)	0.39	0.035500	-0.000090	0.000002	0.01	0.0017	0.0000
Calcite ($Ce^{4+}Ca_{62}C_{64}O_{192}$)	0.50	0.045500	-0.000090	0.000002	0.01	0.0015	$-9*10^{-16}$
Minerals	$10^3\ln^{142/136}\alpha_{Mass}$ at 300K	a	b	c	$10^3\ln^{142/136}\alpha_{NVE}$ at 300K	a	b
Cerianite	-0.1	-0.0167	0.0009	0.000020	-0.58	-0.1727	$-1*10^{-16}$
Monazite	0.57	0.0491	0.0003	-0.000009	-0.16	-0.0468	$-3*10^{-16}$
Percleveite	0.78	0.0689	0.0002	-0.00001	-0.22	-0.0649	$-8*10^{-16}$
Calcite ($Ce^{3+}NaCa_{62}C_{64}O_{192}$)	1.13	0.104	-0.0003	0.000006	-0.79	-0.2375	$-1*10^{-16}$
Calcite ($Ce^{4+}Ca_{62}C_{64}O_{192}$)	1.46	0.1337	-0.0003	0.000007	-0.86	-0.2591	$-3*10^{-16}$
Minerals	$10^3\ln^{142/140}\alpha_{Mass}$ at 300K	a	b	c	$10^3\ln^{142/140}\alpha_{NVE}$ at 300K	a	b
Cerianite	-0.03	-0.005400	0.000300	-0.000007	-0.52	-0.1556	$-2*10^{-16}$
Monazite	0.18	0.015900	0.000090	-0.000003	-0.14	-0.0421	$-6*10^{-16}$
Percleveite	0.25	0.022300	0.000080	-0.000004	-0.19	-0.0583	$-3*10^{-16}$
Calcite ($Ce^{3+}NaCa_{62}C_{64}O_{192}$)	0.37	0.033900	-0.000090	0.000002	-0.78	-0.2333	$-1*10^{-16}$
Calcite ($Ce^{4+}Ca_{62}C_{64}O_{192}$)	0.48	0.043600	-0.000090	0.000002	-0.71	-0.2139	$-1*10^{-16}$

$10^3\ln\alpha_{Mass} = ax + bx^2 + cx^3+d$, where x is $10^6/ T^2$.

$10^3\ln\alpha_{NVE} = ax + bx^2$, where x is $10^3/ T$.

Table S-3 Ce isotope fractionation ($\Delta^{142/140}Ce$) during the deposition of manganite oxides (M), phosphate (P), and carbonate (C) in seawater with pH of ca. 8 (SW).

Oxidised Ocean		Anaerobic Ocean	
Seawater	Negative Ce* & $\Delta^{142/140}Ce$ = + 0.4‰ (SW/M)	Seawater	None Ce* & $\Delta^{142/140}Ce$ = - 0.34‰ (SW/P)
Manganite nodule	Positive Ce* & $\Delta^{142/140}Ce$ = - 0.4‰ (M/SW)	Phosphate	None Ce* & $\Delta^{142/140}Ce$ = + 0.34‰ (P/SW)
Carbonate	Negative Ce* & $\Delta^{142/140}Ce$ = 0.11‰ to -0.7‰ (SW/C)	Carbonate	None Ce* & $\Delta^{142/140}Ce$ = 0.11‰ to -0.7‰ (SW/C)

Supplementary Figures

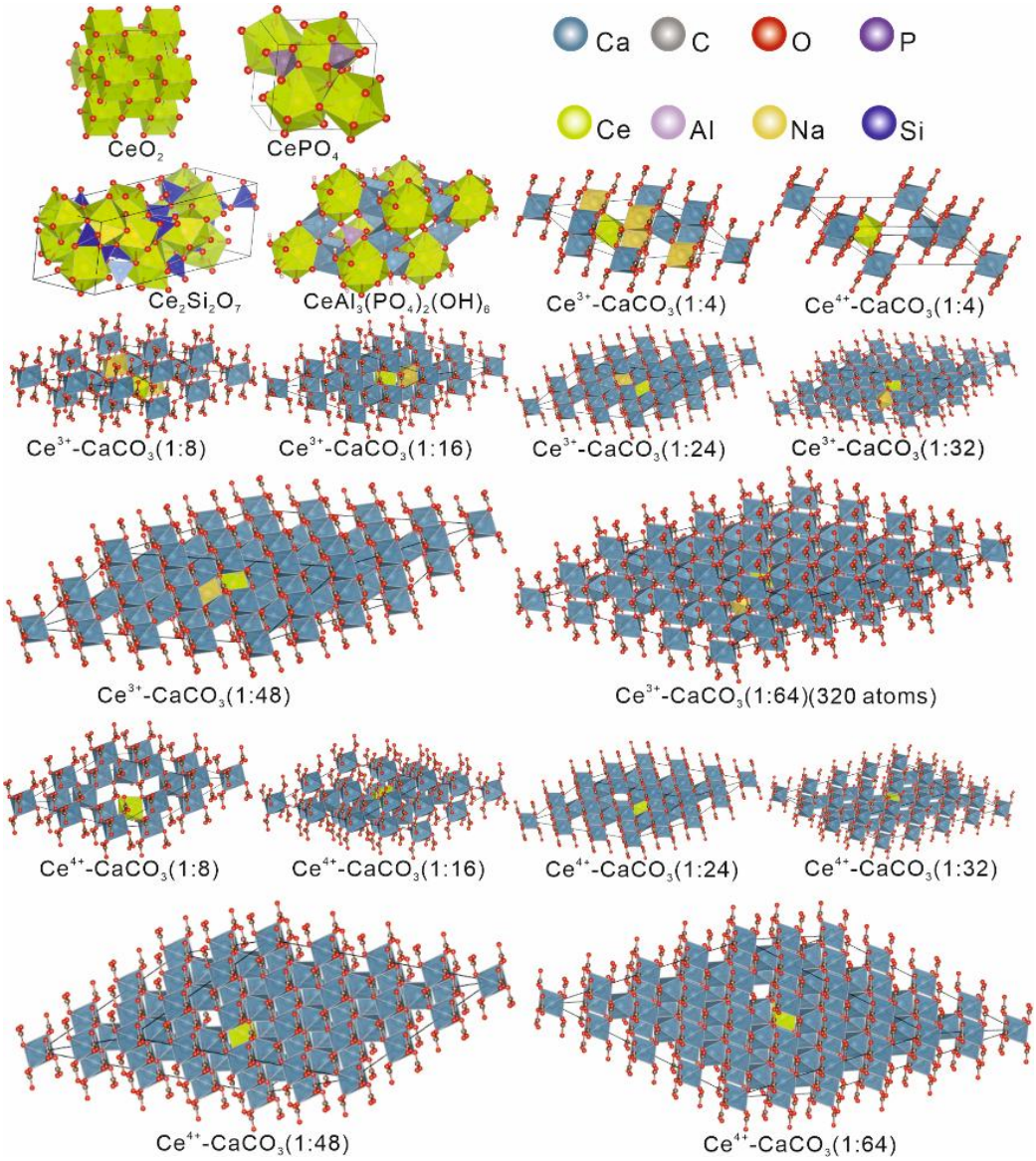

Figure S-1 Optimised mineral structures for Ce-bearing minerals. These minerals include cerianite (CeO_2), percleveite ($Ce_2Si_2O_7$), monazite ($CePO_4$), florencite ($CeAl_3(PO_4)_2(OH)_6$), and Ce^{3+}-doped calcites and Ce^{4+}-doped calcites, including $Ce^{3+}NaCa_2C_4O_{12}$, $Ce^{3+}NaCa_6C_8O_{24}$, $Ce^{3+}NaCa_{14}C_{16}O_{48}$, $Ce^{3+}NaCa_{22}C_{24}O_{72}$, $Ce^{3+}NaCa_{22}C_{24}O_{72}$, $Ce^{3+}NaCa_{30}C_{32}O_{96}$, $Ce^{3+}NaCa_{46}C_{48}O_{144}$, $Ce^{3+}NaCa_{62}C_{64}O_{192}$, $Ce^{4+}Ca_2C_4O_{12}$, $Ce^{4+}Ca_6C_8O_{24}$, $Ce^{4+}Ca_{14}C_{16}O_{48}$, $Ce^{4+}Ca_{22}C_{24}O_{72}$, $Ce^{4+}Ca_{22}C_{24}O_{72}$, $Ce^{4+}Ca_{30}C_{32}O_{96}$, $Ce^{4+}Ca_{46}C_{48}O_{144}$, and $Ce^{4+}Ca_{62}C_{64}O_{192}$. Ce cations are shown in luminous yellow. All these mineral structures analyses were

conducted using the software ‘‘VESTA” (Momma and Izumi, 2008). The original structures were obtained from experimental results (see Fig. S-1 for their data sources).

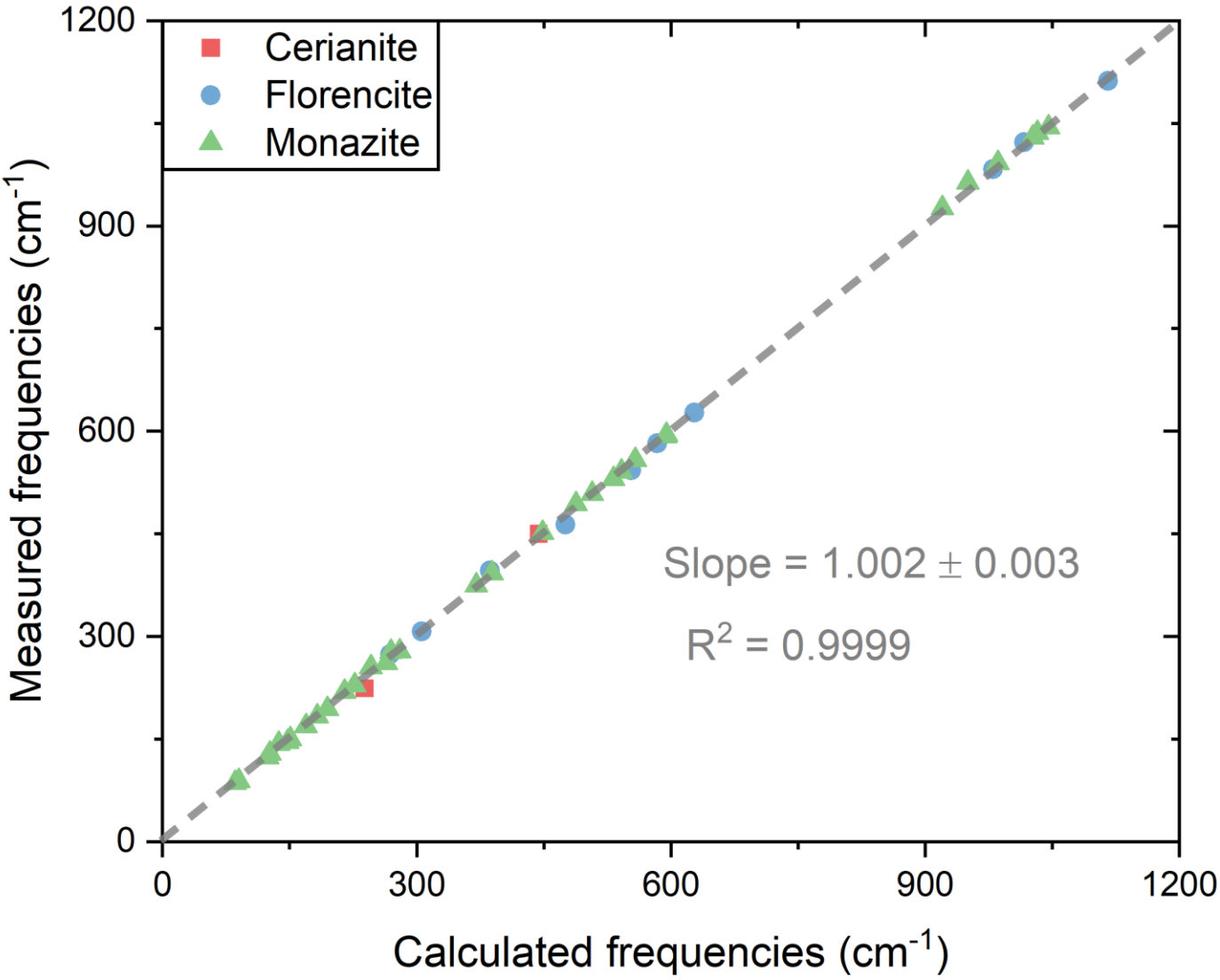

Figure S-2 Linear fitting of vibrational frequencies between calculations and experiments. Although the structures of cerianite, percleveite, monazite, florencite, and Ce^{3+}-doped calcites and Ce^{4+}-doped calcites have been constrained by experiments (Graham, 1955; Ni *et al*., 1995; Kato, 1990; Deng and Ibers, 2005; Antao and Hassan, 2010), the vibrational frequencies of some minerals have yet to be measured. The experimental vibrational frequencies are collected from Errandonea *et al*. (2018), Zhukova *et al*. (2023), and Ghignone *et al.* (2024).

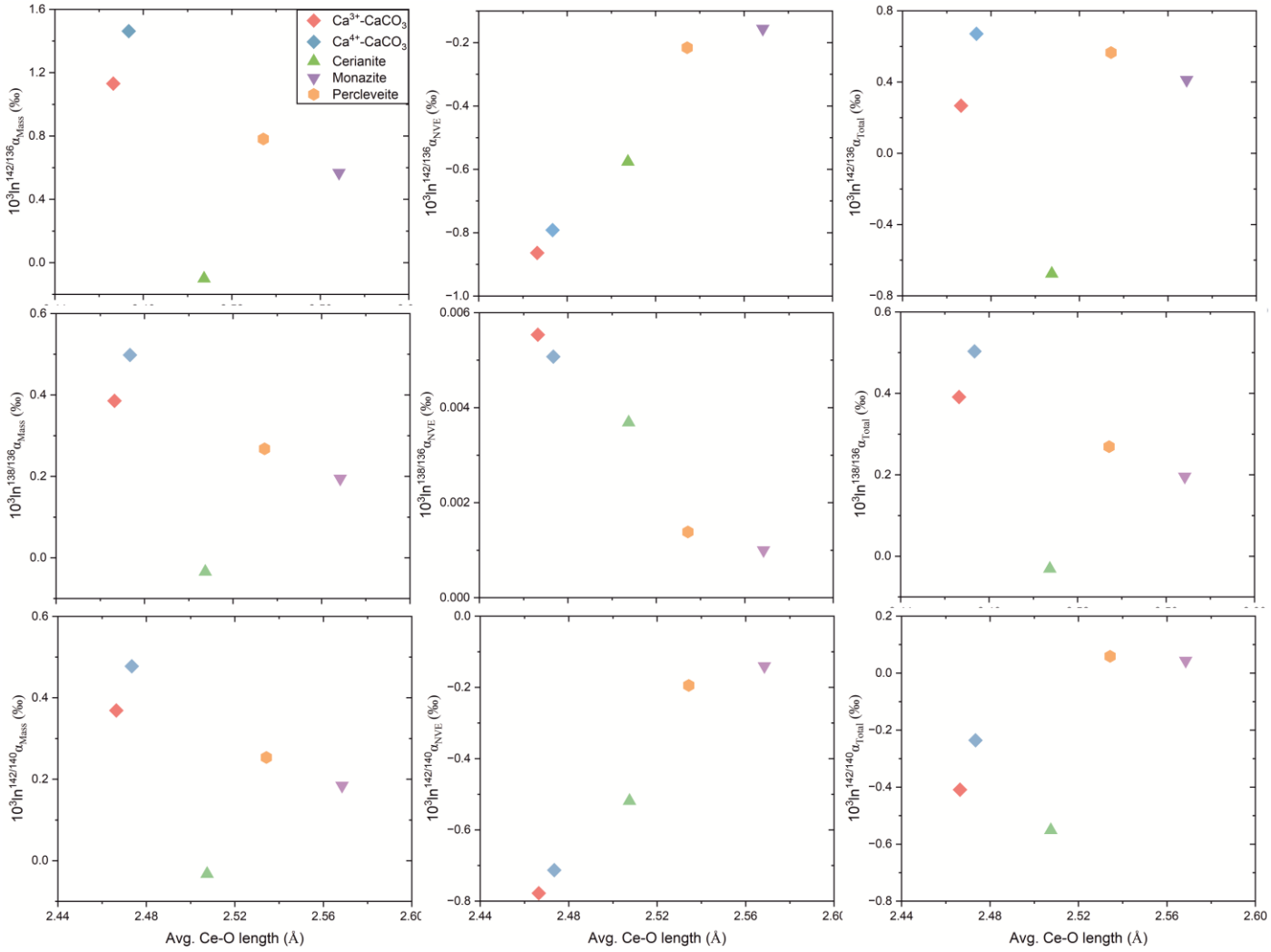

Figure S-3 The $10^3 ln\alpha_{Mass}$, $10^3 ln\alpha_{NVE}$ and $10^3 ln\alpha_{Total}$ versus the average length of Ce-O at 300 K.

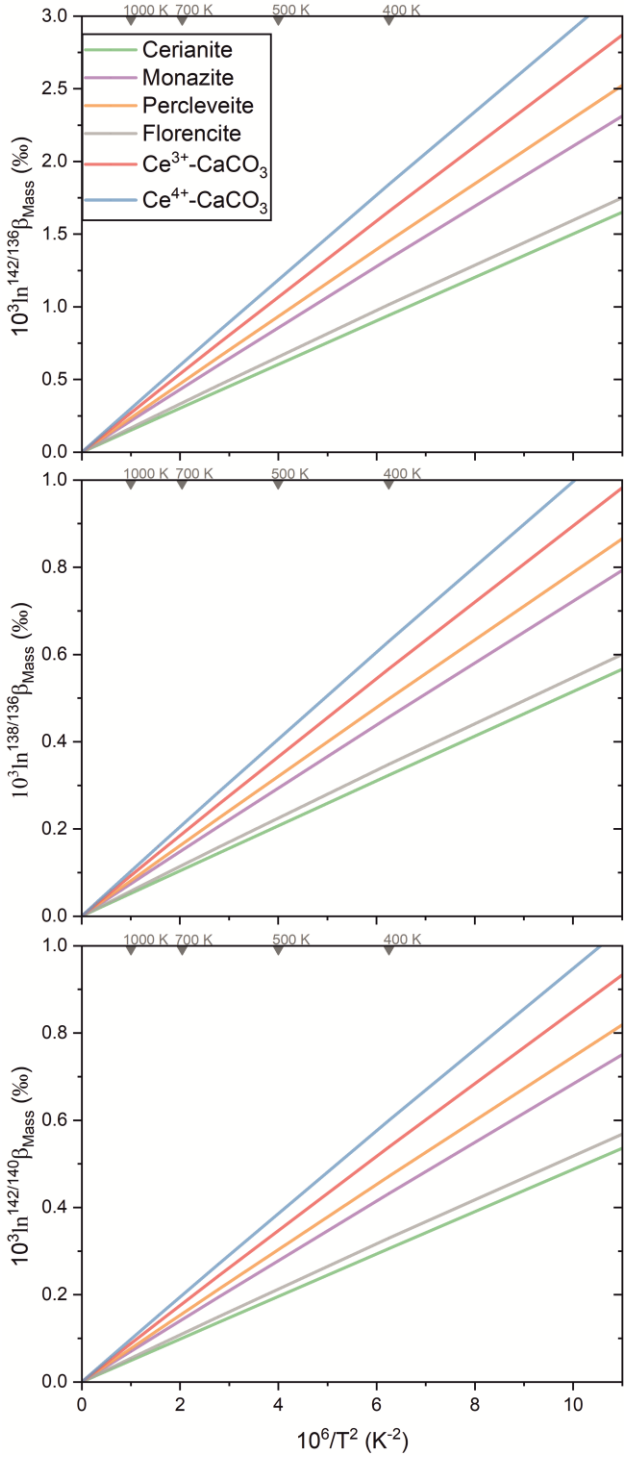

Figure S-4 Calculated reduced partition function ratios ($10^3 ln\beta$) varying with temperature ($10^6/T^2$) for Ce-bearing minerals. At the same temperature, the values of $10^3 ln^{138/136}\beta_{Mass}$, $10^3 ln^{142/136}\beta_{Mass}$, and $10^3 ln^{142/140}\beta_{Mass}$ increase in the following sequence of cerianite < florencite < monazite < percleveite < Ce^{3+}-doped calcite < Ce^{4+}-doped calcite.

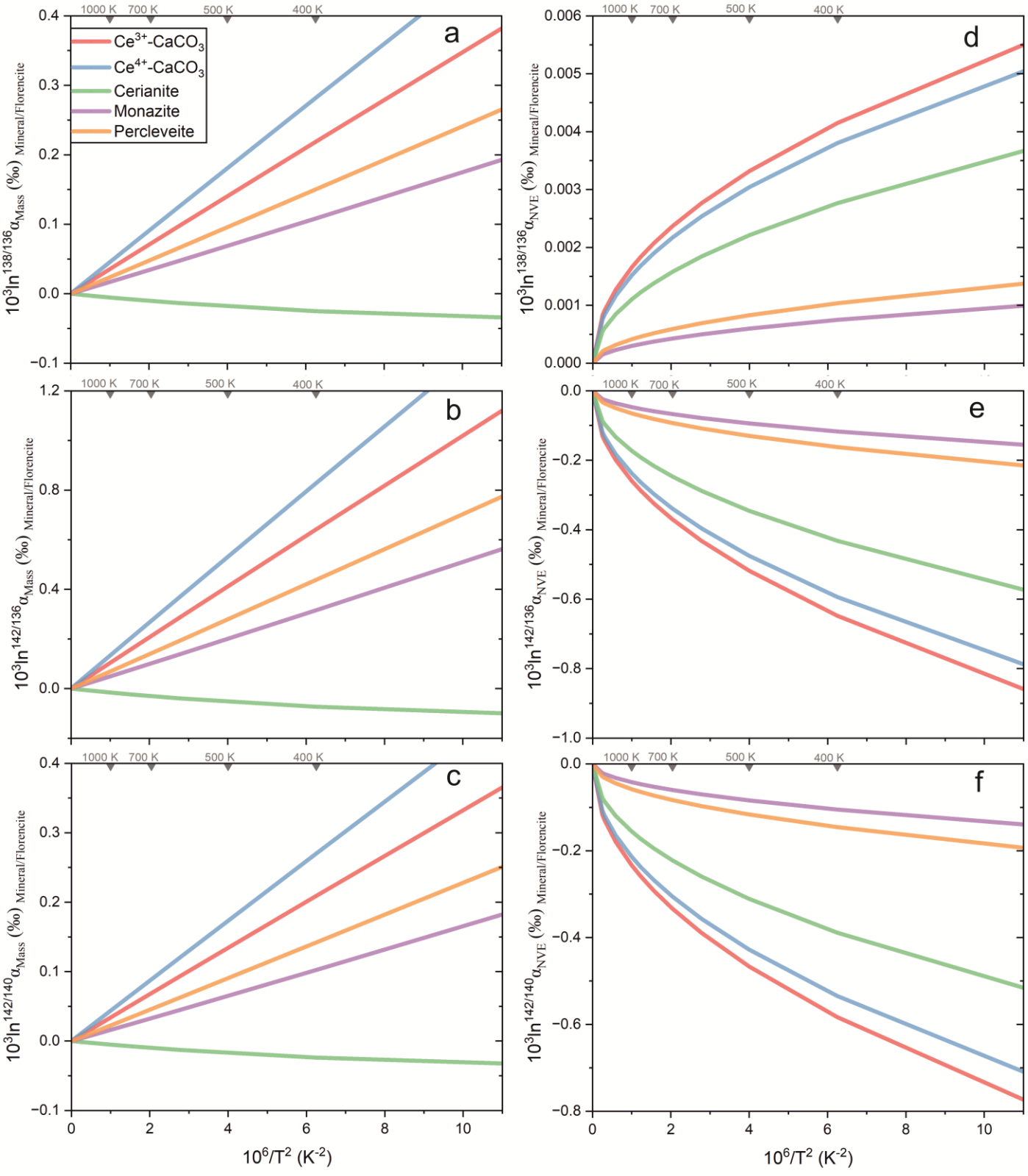

Figure S-5 The mass-dependent and mass-independent equilibrium Ce isotope fractionation factor ($10^3 ln\alpha_{Mass}$ & $10^3 ln\alpha_{NVE}$) between minerals and florencite. At the same temperature, $10^3 ln^{138/136}\alpha_{Mass}$, $10^3 ln^{142/136}\alpha_{Mass}$, and

$10^3 ln^{142/140}\alpha_{Mass}$ increase in the following sequence of cerianite < monazite < percleveite < Ce^{3+}-doped calcite < Ce^{4+}-doped calcite. At the same temperature, $10^3 ln^{138/136}\alpha_{NVE}$ decreases in the following sequence of Ce^{3+}-doped calcite < Ce^{4+}-doped calcite < cerianite < percleveite < monazite. In contrast, the $10^3 ln^{142/136}\alpha_{NVE}$ and $10^3 ln^{142/140}\alpha_{NVE}$ decreases in the following sequence of monazite < percleveite < cerianite < Ce^{4+}-doped calcite < Ce^{3+}-doped calcite.

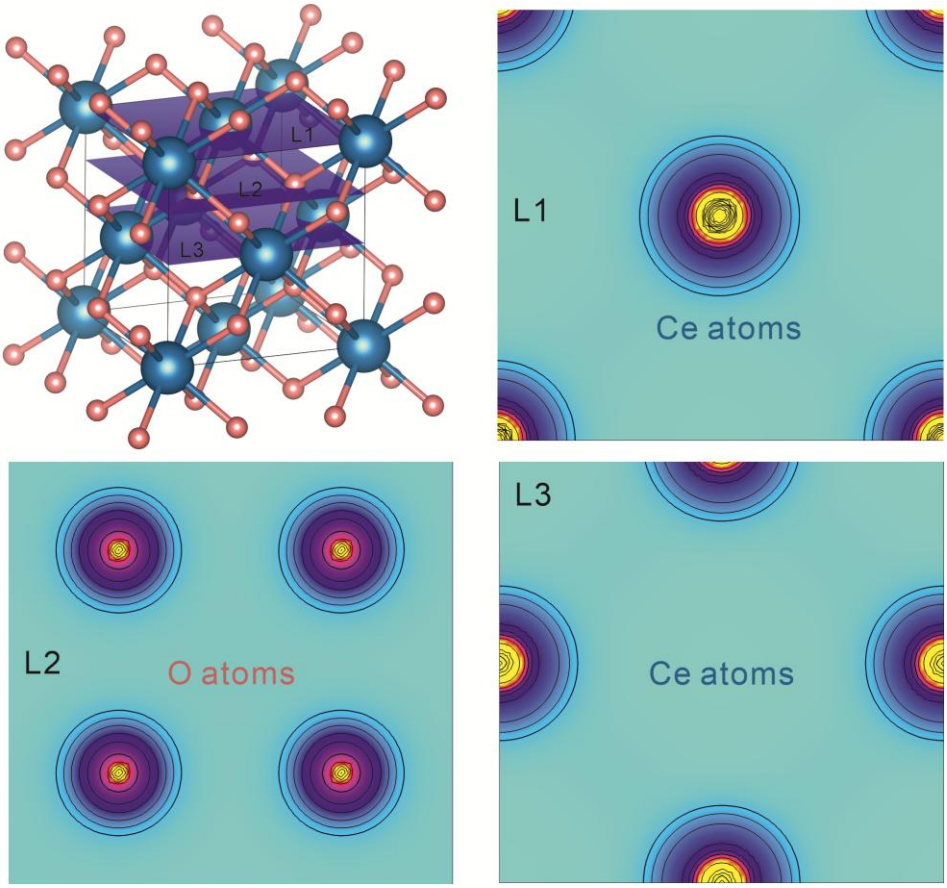

Figure S-6 Electron density at the nuclei of cerianite. The electron density of Ce is several orders of magnitude greater than that of O.

Supplementary Information References

Almoukhalalati, A., Shee, A., Saue, T. (2016) Nuclear size effects in vibrational spectra. *Physical Chemistry Chemical Physics* 18, 15406–15417. https://doi.org/10.1039/C6CP01913G

Antao, S.M., Hassan, I. (2010) Temperature dependence of the structural parameters in the transformation of aragonite to calcite, as determined from in situ synchrotron powder X-ray-diffraction data. *The Canadian Mineralogist* 48, 1225–1236. https://doi.org/doi:10.3749/canmin.48.5.1225

Baroni, S., Giannozzi, P., Testa, A. (1987) Green's-function approach to linear response in solids. *Physical Review Letters* 58, 1861–1864. https://doi.org/10.1103/PhysRevLett.58.1861

Bigeleisen, J. (1996) Nuclear Size and Shape Effects in Chemical Reactions. Isotope Chemistry of the Heavy Elements. *Journal of the American Chemical Society* 118, 3676–3680. https://doi.org/10.1021/ja954076k

Bigeleisen, J., Mayer, M.G. (1947) Calculation of equilibrium constants for isotopic exchange reactions. *The Journal of Chemical Physics* 15, 261–267. https://doi.org/10.1063/1.1746492

Blanchard, M., Morin, G., Lazzeri, M., Balan, E. (2010) First-principles study of the structural and isotopic properties of Al- and OH-bearing hematite. *Geochimica et Cosmochimica Acta* 74, 3948–3962. https://doi.org/10.1016/j.gca.2010.04.018

Dal Corso, A. (2014) Pseudopotentials periodic table: From H to Pu. *Computational Materials Science* 95, 337–350. https://doi.org/10.1016/j.commatsci.2014.07.043

Dauphas, N., Schauble, E.A. (2016) Mass Fractionation Laws, Mass-Independent Effects, and Isotopic Anomalies. *Annual Review of Earth and Planetary Sciences* 44, 709–783. https://doi.org/10.1146/annurev-earth-060115-012157

Dauphas, N., Roskosz, M., Alp, E.E., Neuville, D.R., Hu, M.Y., Sio, C.K., Tissot, F.L.H., Zhao, J., Tissandier, L., Médard, E., Cordier, C. (2014) Magma redox and structural controls on iron isotope variations in Earth's mantle and crust. *Earth and Planetary Science Letters* 398, 127–140. https://doi.org/10.1016/j.epsl.2014.04.033

Deng, B., Ibers, J.A. (2005) Dicerium disilicate, $Ce_2[Si_2O_7]$. *Acta Crystallographica Section E: Structure Reports Online* 61, 76–78. https://doi.org/10.1107/S1600536805011049

Duan, H., Huang, F. (2024) Equilibrium indium isotope fractionation between indium-bearing minerals: Insights from first-principles calculations. *Geochimica et Cosmochimica Acta* 369, 51–61. https://doi.org/10.1016/j.gca.2024.01.031

Duan, H., Yang, B., Huang, F. (2023) Site-specific isotope effect: Insights from equilibrium magnesium isotope fractionation in mantle minerals. *Geochimica et Cosmochimica Acta* 357, 13–25. https://doi.org/10.1016/j.gca.2023.05.014

Errandonea, D., Gomis, O., Rodríguez-Hernández, P., Muñoz, A., Ruiz-Fuertes, J., Gupta, M., Achary, S.N., Hirsch, A., Manjon, F.J., Peters, L., Roth, G., Tyagi, A.K., Bettinelli, M. (2018) High-pressure structural and vibrational properties of monazite-type $BiPO_4$, $LaPO_4$, $CePO_4$, and $PrPO_4$. *Journal of Physics: Condensed Matter* 30, 065401. https://doi.org/10.1088/1361-648X/aaa20d

Ghignone, S., Prencipe, M., Manzotti, P., Bruno, M., Boero, F., Borghini, A., Costa, E., Ciriotti, M., Scaramuzzo, E. (2024) The Raman spectrum of florencite-(REE) [$REEAl_3(PO_4)_2(OH)_6$]: An integrated experimental and computational approach. *Journal of Raman Spectroscopy* 55, 394–405. https://doi.org/10.1002/jrs.6640

Giannozzi, P., Andreussi, O., Brumme, T., Bunau, O., Nardelli, M.B. *et al.* (2017) Advanced capabilities for materials modelling with Quantum ESPRESSO. *Journal of Physics: Condensed Matter* 29, 465901. https://doi.org/10.1088/1361-648X/aa8f79

Graham, A.R. (1955) Cerianite CeO_2: A new rare-earth oxide mineral. *American Mineralogist* 40, 560–564. https://doi.org/ammin/AM40/AM40_560.pdf

Hamann, D.R. (2013) Optimized norm-conserving Vanderbilt pseudopotentials. *Physical Review B* 88, 085117. https://doi.org/10.1103/PhysRevB.88.085117

Hoefs, J. (2009) Stable Isotope Geochemistry, 6th ed. *Springer-Verlag*, Berlin Heidelberg. https://doi.org/10.1007/978-3-540-70708-0

Kato, T. (1990) The crystal structure of florencite. *Neues Jahrbuch für Mineralogie, Monatshefte* 5, 227–231.

Kresse, G., Joubert, D. (1999) From ultrasoft pseudopotentials to the projector augmented-wave method. *Physical Review B* 59, 1758–1775. https://doi.org/10.1103/PhysRevB.59.1758

Liu, S., Li, Y., Yang, Z., Liu, J. (2023) Fe isotope fractionation caused by phase transition of FeS and implications for Fe isotope signatures of the mantle and core. *Geochimica et Cosmochimica Acta* 340, 38–50. https://doi.org/10.1016/j.gca.2022.10.042

Méheut, M., Lazzeri, M., Balan, E., Mauri, F. (2009) Structural control over equilibrium silicon and oxygen isotopic fractionation: A first-principles density-functional theory study. *Chemical Geology*, Applications of non-traditional stable isotopes in high-temperature geochemistry 258, 28–37. https://doi.org/10.1016/j.chemgeo.2008.06.051

Momma, K., Izumi, F. (2008) VESTA: a three-dimensional visualization system for electronic and structural analysis. *Journal of Applied Crystallography* 41, 653–658. https://doi.org/10.1107/S0021889808012016

Morales-García, Á., Rhatigan, S., Nolan, M., Illas, F. (2020) On the use of DFT+U to describe the electronic structure of TiO_2 nanoparticles: $(TiO_2)_{35}$ as a case study. *The Journal of Chemical Physics* 152, 244107. https://doi.org/10.1063/5.0012271

Nemoto, K., Abe, M., Seino, J., Hada, M. (2015) An ab initio study of nuclear volume effects for isotope fractionations using two-component relativistic methods. *Journal of Computational Chemistry* 36, 816–820. https://doi.org/10.1002/jcc.23858

Ni, Y., Hughes, J.M., Mariano, A.N. (1995) Crystal chemistry of the monazite and xenotime structures. *American Mineralogist* 80, 21–26. https://doi.org/doi:10.2138/am-1995-1-203

Perdew, J.P., Burke, K., Ernzerhof, M. (1996) Generalized gradient approximation made simple. *Physical Review Letters* 77, 3865–3868. https://doi.org/10.1103/PhysRevLett.77.3865

Pinilla, C., de Moya, A., Rabin, S., Morard, G., Roskosz, M., Blanchard, M. (2021) First-principles investigation of equilibrium iron isotope fractionation in Fe1−xSx alloys at Earth's core formation conditions. *Earth and Planetary Science Letters* 569, 117059. https://doi.org/10.1016/j.epsl.2021.117059

Rabin, S., Blanchard, M., Pinilla, C., Poitrasson, F., Gregoire, M. (2021) First-principles calculation of iron and silicon isotope fractionation between Fe-bearing minerals at magmatic temperatures: The importance of second atomic neighbors. *Geochimica et Cosmochimica Acta* 304, 101–118. https://doi.org/10.1016/j.gca.2021.03.028

Rabin, S., Blanchard, M., Pinilla, C., Poitrasson, F., Grégoire, M. (2023) Iron and silicon isotope fractionation in silicate melts using first-principles molecular dynamics. *Geochimica et Cosmochimica Acta* 343, 212–233. https://doi.org/10.1016/j.gca.2022.11.017

Schauble, E.A. (2007) Role of nuclear volume in driving equilibrium stable isotope fractionation of mercury, thallium, and other very heavy elements. *Geochimica et Cosmochimica Acta* 71, 2170–2189. https://doi.org/10.1016/j.gca.2007.02.004

Schauble, E.A. (2011) First-principles estimates of equilibrium magnesium isotope fractionation in silicate, oxide, carbonate and hexaaquamagnesium(2+) crystals. *Geochimica et Cosmochimica Acta* 75, 844–869. https://doi.org/10.1016/j.gca.2010.09.044

Schauble, E.A. (2013) Modeling nuclear volume isotope effects in crystals. *Proceedings of the National Academy of Sciences* 110, 17714–17719. https://doi.org/10.1073/pnas.1216216110

Schauble, E.A. (2023) Nuclear volume isotope fractionation of europium and other lanthanide elements. *Geochemical Journal* 57, 118–133. https://doi.org/10.2343/geochemj.GJ23010

Son, S., Li, W., Lee, J.-Y., Kwon, K.D. (2020) On the coordination of Mg^{2+} in aragonite: Ab-initio absorption spectroscopy and isotope fractionation study. *Geochimica et Cosmochimica Acta* 286, 324–335. https://doi.org/10.1016/j.gca.2020.07.023

Urey, H.C. (1947) The thermodynamic properties of isotopic substances. *Journal of the Chemical Society* Resumed, 562–581. https://doi.org/10.1039/JR9470000562

Wang, W., Liu, J., Yang, H., Dorfman, S.M., Lv, M., Li, J., Zhu, F., Zhao, J., Hu, M.Y., Bi, W., Alp, E.E., Xiao, Y., Wu, Z., Lin, J.-F. (2021) Iron force constants of bridgmanite at high pressure: Implications for iron isotope fractionation in the deep mantle. *Geochimica et Cosmochimica Acta* 294, 215–231. https://doi.org/10.1016/j.gca.2020.11.025

Xiao, Z.-C., Zhou, C., Kang, J.-T., Wu, Z.-Q., Huang, F. (2022) The factors controlling equilibrium inter-mineral Ca isotope fractionation: insights from first-principles calculations. *Geochimica et Cosmochimica Acta* 333, 373–389. https://doi.org/10.1016/j.gca.2022.07.021

Young, E.D., Manning, C.E., Schauble, E.A., Shahar, A., Macris, C.A., Lazar, C., Jordan, M. (2015) High-temperature equilibrium isotope fractionation of non-traditional stable isotopes: Experiments, theory, and applications. *Chemical Geology* 395, 176–195. https://doi.org/10.1016/j.chemgeo.2014.12.013

Zhukova, I.A., Stepanov, A.S., Malyutina, A., Doroshkevich, A.G., Korsakov, A.V., Jiang, S.-Y., Bakovets, V.V., Pomelova, T.A., Nigmatulina, E.N. (2023) Raman spectroscopic study of non-stoichiometry in cerianite from critical zone. *Journal of Raman Spectroscopy* 54, 1191–1200. https://doi.org/10.1002/jrs.6557